RESEARCH ARTICLE SUMMARY

GEOCHEMISTRY

# Deep abiotic weathering of pyrite

Xin Gu*, Peter J. Heaney, Fabio D. A. Aarão Reis, Susan L. Brantley

**INTRODUCTION:** Oxidative weathering of pyrite, the most abundant sulfide mineral in Earth's crust, is coupled to the biogeochemical cycles of sulfur, oxygen, carbon, and iron. Pyrite oxidation is key to these cycles because of its high reactivity with oxygen. Before the Great Oxidation Event (GOE), atmospheric oxygen concentrations were low on early Earth and pyrite was exposed at Earth's surface, allowing erosion into sediments that were preserved in river deposits. Today, it oxidizes at depth in most rocks and is often not exposed at the land surface. To understand pyrite weathering through geologic time, researchers extrapolate the reaction kinetics based on studies from the laboratory or in acid mine drainage. Such work has emphasized the important role of microorganisms in catalyzing pyrite oxidation. But to interpret the oxidation rates of pyrite on early Earth requires knowledge of the rate-limiting step of the oxidation as it occurs naturally in rocks.

**RATIONALE:** We investigated the oxidation of pyrite in micrometer-sized grains, in centimeter-sized rock fragments, and in meter-scale boreholes at a small, well-studied catchment in a critical-zone observatory. Our goal was to determine the reaction mechanism of pyrite weathering in rocks as it occurs today. The slow-eroding catchment is underlain by shale, the most common rock type exposed on Earth. We determined weathering profiles of pyrite through chemical and microscopic analysis.

**RESULTS:** At the ridgelines of the shale watershed, most pyrite oxidation occurs within a 1-m-thick reaction zone ~16 m below land surface, just above the depth of water table fluctuation. This is the reaction front at the borehole scale. Only limited oxidation occurs in halos around a few fractures at deeper depths. Above the depth where pyrite is 100% oxidized in all boreholes, rock fracture density and porosity are generally higher than below. However, the narrow parts of pore openings called pore throats remain small enough in oxidizing shale to limit access of microorganisms to the pyrite surface. During oxidation, iron oxides pseudomorphically replace the pyrite grains. High-resolution transmission electron microscopy (TEM) reveals that the oxidation front at grain scale is defined by a sharp interface between pyrite and an iron (oxyhydr)oxide (Fh) that is either ferrihydrite or feroxyhyte. This Fh then transforms into a banded structure of iron oxides that ultimately alter to goethite in outer layers. This complex oxidative transformation progresses inward from fractures when observed at clast scale.

**CONCLUSION:** Under today's atmosphere, pyrite oxidation, rate-limited by diffusion of oxygen at the grain scale, is regulated by fracturing at clast scale. As pyrite is oxidized at borehole scale before reaching the land surface in most landscapes today, the oxidation rate is controlled by the movement of pyrite upward, which is in turn limited by the rate of erosion. Comparisons of shale landscapes with different erosion rates reveal that fracture spacing varies with erosion rate, so this suggests that fracture spacing may couple the landscape-scale to grain-scale rates. Microbial acceleration of oxidation globally today is unlikely in low-porosity rocks because pyrite oxidation usually occurs at depth, where pore throats limit access, as observed here for shales. Before the GOE, the rate of pyrite oxidation was instead controlled by the slower reaction kinetics in the presence of lower atmospheric oxygen concentrations. At that time, therefore, pyrite was exposed at the land surface, where microbial interaction could have accelerated the oxidation and acidified the landscape, as suggested by others. Our work highlights the importance of fracturing and erosion in addition to atmospheric oxygen as a control on the reactivity of this ubiquitous iron sulfide. ■

The list of author affiliations is available in the full article online.
*Corresponding author. Email: xug102@psu.edu
Cite this article as X. Gu *et al.*, *Science* **370**, eabb8092 (2020). DOI: 10.1126/science.abb8092

READ THE FULL ARTICLE AT
https://doi.org/10.1126/science.abb8092

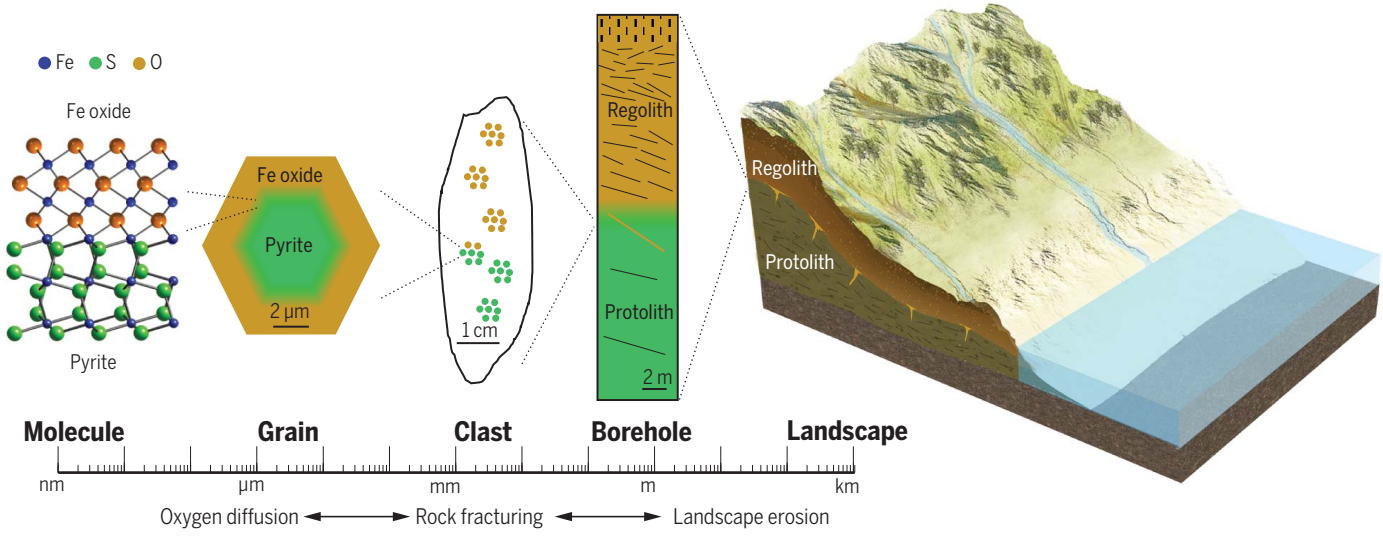


**Schematic depiction of oxidative weathering of pyrite in rocks buried at meters depth.** Pyrite oxidation was studied from the molecular (TEM) scale of the pyrite–Fe oxide interface through clast and borehole scales to extrapolate to landscapes. The rate of oxidation of pyrite, limited at grain scale by oxygen diffusion through the shale matrix, is regulated at larger scales by fracturing and erosion.

RESEARCH ARTICLE

GEOCHEMISTRY

# Deep abiotic weathering of pyrite

Xin Gu[1]*, Peter J. Heaney[1], Fabio D. A. Aarão Reis[2], Susan L. Brantley[1,3]

Pyrite is a ubiquitous iron sulfide mineral that is oxidized by trace oxygen. The mineral has been largely absent from global sediments since the rise in oxygen concentration in Earth's early atmosphere. We analyzed weathering in shale, the most common rock exposed at Earth's surface, with chemical and microscopic analysis. By looking across scales from $10^{-9}$ to $10^{2}$ meters, we determined the factors that control pyrite oxidation. Under the atmosphere today, pyrite oxidation is rate-limited by diffusion of oxygen to the grain surface and regulated by large-scale erosion and clast-scale fracturing. We determined that neither iron- nor sulfur-oxidizing microorganisms control global pyrite weathering fluxes despite their ability to catalyze the reaction. This multiscale picture emphasizes that fracturing and erosion are as important as atmospheric oxygen in limiting pyrite reactivity over Earth's history.

Pyrite is an extremely reactive, abundant sulfide in Earth's crust, and its oxidation is an important regulator of biogeochemical processes (*1*). Oxidative weathering of pyrite (OWP) is coupled to the global budgets of four of the most common redox-active elements on Earth: sulfur, oxygen, carbon, and iron (*2*–*6*). OWP releases ~45% of the world's freshwater flux of sulfur to the ocean (*7*), controls reactivity of iron in some groundwaters (*8*, *9*), draws oxygen out of the atmosphere (*10*), and couples with the carbon cycle (*11*, *12*).

OWP is particularly important to our understanding of Earth's dynamic oxygenation history (*13*, *14*). For example, the presence or absence of detrital pyrite in preserved sediments reflects the intensity of terrestrial OWP and can therefore be a record of oxygen in the early atmosphere (*2*, *15*, *16*). In addition, when terrestrial OWP increased during the Great Oxidation Event (GOE) at ~2.5 billion years (Gyr) ago, it likely generated acid that in turn affected the balance of some nutrients and trace metals in the ocean (*17*, *18*). Overall, OWP is an important process in the negative feedback that may promote the stabilization of oxygen partial pressure ($pO_2$) in the atmosphere (*19*, *20*).

Explanations of OWP in Earth's past rely on extrapolations of pyrite oxidation kinetics to low $pO_2$ and on assumptions that the rate of OWP is proportional to $pO_2$ (*19*, *20*). This latter assumption is key because extrapolation implicitly requires knowledge of rate-limiting steps. If the mechanism changes, this extrapolation is no longer valid. Previous research on pyrite reactivity focused on oxidation in the laboratory [e.g., (*21*–*23*)] or in acid mine drainage (*24*, *25*). In acid mine drainage, the rate-limiting step is oxidation of aqueous Fe(II) to Fe(III) because Fe(III) is a more efficient oxidant than $O_2$ in acidic conditions (*21*, *22*, *24*). In addition, under acidic or circumneutral pH, OWP can be accelerated by more than one order of magnitude by some iron- and sulfur-oxidizing microorganisms living on or near the mineral surface (*26*–*28*).

Owing to the high concentration of $O_2$ in the modern atmosphere and high reactivity of pyrite, OWP today is suggested to be limited by erosion (*2*) rather than interfacial reaction. This idea is supported by observations showing that the flux of OWP-generated sulfate is proportional to the rate of erosion in some catchments (*29*, *30*). In addition, several researchers have documented cases where pyrite oxidizes to a depth of meters in pyrite-rich black shales (*31*–*34*), pyrite-poor shales (*30*, *35*–*38*), and crystalline rocks (*39*).

Although pyrite has been documented in isolated occurrences to oxidize at meters to tens of meters below the land surface, the controls on deep reactivity are still poorly understood (*40*). We do not know if microorganisms facilitate oxidation reactions at these depths, whether the reaction is oxidant-limited, and how these controls may have changed through time. To answer these questions, we integrated observations from pyrite grains to rock fragments to boreholes in a shale watershed (Fig. 1). Using images and analyses from $10^{-9}$ to $10^{2}$ m, we explore the implications of multiscale reactivity for the global oxygen and sulfur cycles (*3*–*5*).

We study shales because they are the most common rock exposed on Earth and because they are pyrite-containing but low in porosity, like most exposed igneous and metamorphic rocks (*2*, *11*). Our focus is a watershed where erosional and hydrological processes are well studied (*41*). This watershed (Shale Hills, Pennsylvania, USA) is slow-eroding but can nonetheless elucidate global OWP because it exhibits some of the same features of OWP observed in shales experiencing some of the highest rainfall and erosion rates in the world (*30*).

### Pyrite measured in boreholes

At Shale Hills, layers of weathered material (regolith) overlie the parent shale (protolith). Regolith consists of a thin soil (0.2 to 3 m) above tens of meters of weathered and fractured rock (15 to 22 m thick). The protolith, a gray Silurian shale, contains trace sulfur in the form of pyrite (*30*). Pyrite occurs as both single euhedral crystals and raspberry-like clusters of euhedral crystals (framboids) disseminated in a clay + quartz matrix. When considered from the perspective of the land surface, regolith forms as protolith is moved up and through the weathering zone while topsoil is removed by erosion. The cumulative effect is recorded over time in regolith as elemental depth profiles, which extend from the most highly weathered material at land surface to protolith at depth (*42*, *43*). We examined weathering profiles in material recovered from boreholes under a ridge and a valley (fig. S1).

Like other shales (*31*–*35*, *38*), the earliest alterations observed at Shale Hills are fracturing, dissolution of carbonate, and OWP (*30*, *36*, *37*). During OWP, iron oxides replace iron sulfide while retaining the external shape. This phenomenon is called pseudomorphism and is exemplified by octahedral Fe (oxyhydr)oxide microcrystals within framboids (Fig. 2). The Fe oxide phases evolved as the pseudomorphs moved upward through the zone of oxidation. We performed transmission electron microscopy (TEM) on samples at different depths and found that ferrihydrite or feroxyhite (Fh) formed initially at the interface with the oxidizing pyrite (Fig. 3) but then was later replaced over time by goethite.

Under the south ridge at Shale Hills (fig. S1), OWP initiates 16 m below the land surface (mbls), defining the distance that oxidation has advanced into the subsurface. We identify this distance, $L_b$, as the thickness of oxidized regolith. We use subscript b to indicate borehole scale (meters) as a contrast to the centimeter scale of a clast (c) or micrometer scale of a grain (g). Pyrite has completely oxidized throughout the layer of thickness $L_b$, except in the bottom ~1-m-thick depth interval ($l_b$) located about 1.5 to 3.5 m above the water table, where oxidation and formation of pseudomorphs are ongoing (Fig. 1A and fig. S2). We determined the change in fractional extent of oxidation versus depth across $l_b$. We identify $l_b$ as the reaction front (Fig. 1A) because pyrite abundance varies generally from deep to shallow as the extent of oxidation varies from 0

[1]Department of Geosciences, The Pennsylvania State University, University Park, PA 16802, USA. [2]Instituto de Física, Universidade Federal Fluminense, Avenida Litorânea s/n, 24210-340 Niterói, RJ, Brazil. [3]Earth and Environmental Systems Institute, The Pennsylvania State University, University Park, PA 16802, USA.
*Corresponding author. Email: xug102@psu.edu

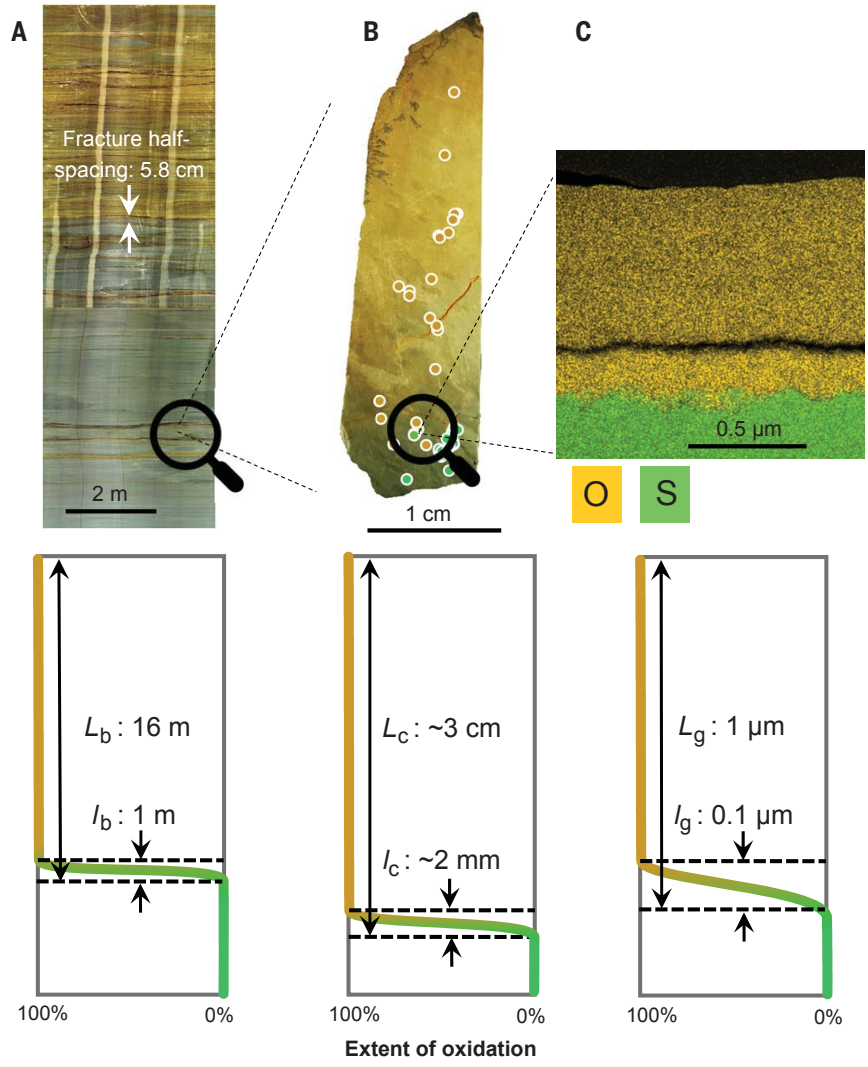


**Fig. 1. Images and schematic depth profiles showing extent of pyrite oxidation at borehole (subscript b), clast (c), and grain (g) scales.** (**A**) Optical downhole televiewer image of a drilled core showing depth to rock containing unaltered pyrite, i.e., oxidation advance distance ($L_b$) and depth interval across which pyrite is oxidizing (the thickness of reaction front, $l_b$) for borehole CZMW8 under south ridge of Shale Hills. (**B**) Optical image of a partially oxidized shale clast formed as a fragment between fractures from the depth shown in (A) (borehole CZMW8, ~25.5 mbls). The small white circles show the locations of pyrite and Fe oxides pseudomorphs. Distance from fracture into unaltered center of fragment, i.e., oxidation advance distance ($L_c$), is shown with the thickness of oxidation front ($l_c$). Extent of oxidation was determined by sulfur concentrations in pyrite and oxide framboids (see Fig. 2), semiquantified from EDS. (**C**) Elemental map (STEM-EDS) of a partially oxidized pyrite grain (green: sulfur; brown: oxygen) collected from the weathered clast as in (B). Thickness of the oxidized rim ($L_g$, i.e., the oxidation advance distance) and thickness of oxidation front ($l_g$) for a partially oxidized pyrite grain. Colors vary with extent of oxidation from green (unoxidized) to orange (oxidized). Dark horizontal line is a zone with high porosity. Extent of oxidation was calculated from the mass transfer coefficient $\tau_{py}$ as described in materials and methods (0% oxidation for $\tau_{py}$ = 0 to 100% for $\tau_{py}$ = −1).

to 100%. We also observed that the advance distance of oxidation at the clast scale ($L_c$) is a few centimeters with a reaction front thickness $l_c$ ~ 2 mm (Fig. 1B), and the advance distance of oxidation at the grain scale ($L_g$) is ~1 μm with $l_g$ ~ 0.1 μm (Fig. 1C). The magnitudes of $L$ and $l$ at all these scales vary with location of borehole in the landscape, depth of clast in the oxidation front, and distance of pyrite grain from the fractured edge of a clast.

As erosion exhumes the shale, porosity grows through dissolution and fracturing (fig. S2). The average fracture density measured by downhole televiewer increases from 3.9 ± 3.0 fractures per meter below the OWP front to 8.7 ± 3.2 fractures per meter (spacing of 5.8 ± 2.5 cm) above the front (measured under the south ridge, fig. S2). The effective porosity (porosity that is open to fluid flow) that we measured by mercury intrusion also increases from 1.6 ± 0.5% of the protolith to 4.5 ± 0.3% of the weathered rock across the front (table S1). The increase in porosity cannot be explained by oxidation of the trace pyrite (~0.2 to 0.3 wt % in protolith). However, as previously documented (*30*, *44*), porosity growth can be largely accounted for by dissolution of chlorite, the most abundant iron-containing clay (13 to 17 wt % in protolith). At the same depth that pyrite becomes ~100% oxidized, dissolution of chlorite begins (*30*, *37*, *44*). Under the valley, we observed similar increases in porosity, fracture density, and degree of chlorite dissolution above the depth that OWP reaches 100% (fig. S3) (*44*).

Although porosity increases upward, the width of pore throats in regolith under the south ridge does not grow larger than 10 to 20 nm as weathering proceeds (*30*). These throats, the narrow parts of pore openings, are important because they are the most restrictive with respect to access of fluids (*45*) and microorganisms (*46*). By contrast, pore throats under the valley at some depths grow larger than 400 nm (table S1). The reason for this larger size is that the sedimentary strata under the valley initially contain more abundant carbonate minerals than under the ridgelines, and the dissolution of these minerals leaves less-constricted pore throats.

### Pyrite weathering in shale fragments

Although we emphasize that most of the OWP occurs in a meter-wide reaction zone under ridgelines, the regolith-protolith interface is not a Euclidean plane but rather a highly rough interface shaped by faults and fractures. This geometry has also been suggested for other low-porosity rocks (*39*, *47*). In our study site, for example, OWP is observed around a few fractures beneath the water table under the ridges (*44*). In one example from an oxidized halo around a fracture, we again observed pyrite + Fe oxides in pseudomorphs (Fig. 2) where oxidation of pyrite is 100% complete at the fracture and decreases to undetectable levels ~3 cm away. This documents the distance that oxidation advanced from the fracture into the clast, $L_c$ (Fig. 2). The width of the reaction front across which pyrite is 100% oxidized at that scale, $l_c$, is constrained by observation to be ~2 mm (Fig. 1B).

We inferred from these observations that, as erosion removes topsoil at the land surface and shale moves closer to the land surface over geologic time, new fractures form and rock fragments or clasts between fractures oxidize progressively inward from their fractured surfaces (fig. S4).

### Pyrite weathering in single grains

We measured the oxidation advance distance $L_g$ in grains within partially pseudomorphed

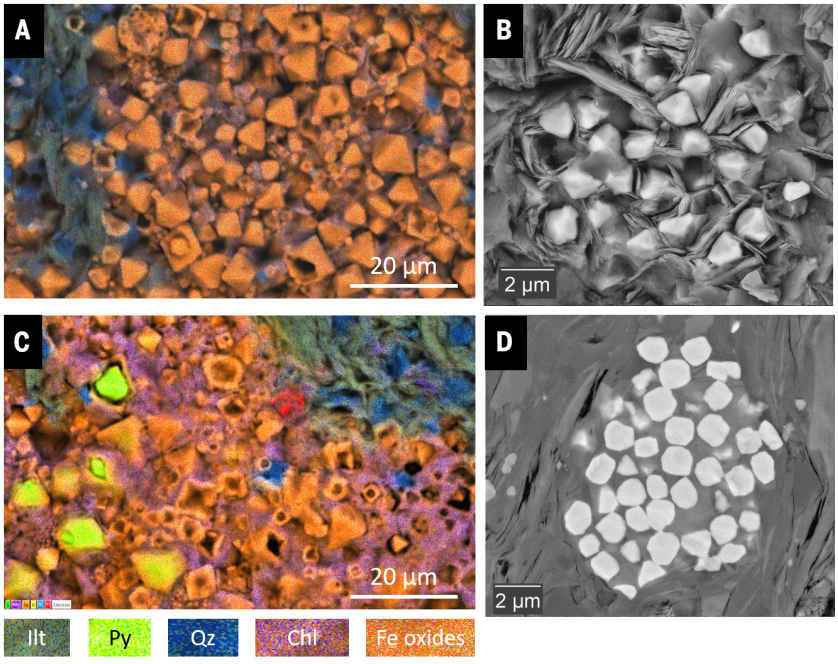


**Fig. 2. Photomicrographs of oxidizing pyrite and its pseudomorphs within one rock fragment shown in Fig. 1B.** (**A**) X-ray elemental map (SEM-EDS) of framboidal and euhedral Fe oxide pseudomorphs after pyrite. (**B**) Back-scattered SEM image of Fe oxide framboid formed in situ in shale as pseudomorph. (**C**) X-ray elemental map (SEM-EDS) of partially oxidized pyrite. (**D**) Back-scattered SEM image of unaltered framboidal pyrite on an ion-milled section of deep unaltered bedrock. Chl: chlorite; Ilt: illite; Py: pyrite; Qz: quartz.

framboids (Fig. 3). Grains (~5 μm in radius) exhibit pyrite cores surrounded by rims of Fe oxides. The sulfur in the crystalline and nonporous pyrite core of grains is progressively replaced by oxygen to form Fh across a sharp interface (Fig. 3B). No sulfate mineral phases are present because sulfur and oxygen are never observed together. Therefore, the concentration profiles of sulfur and oxygen are reciprocal (Fig. 3B and fig. S5). For one specific grain, the depth of penetration of oxidation, $L_g$, is ~1 μm and reaction front thickness, $l_g$, is ~0.1 μm (Fig. 3).

Microscopic characterization reveals that Fh transforms to goethite (Gth) within a complex banded structure that follows the sequence pyrite-Fh-Gth-Fh-Gth (Fig. 3B). As we discovered using high-resolution TEM (HRTEM), unoxidized pyrite is surrounded by a very thin layer (10 to 20 nm) of Fh (Fig. 3C). This first transformation to Fh is consistent with laboratory observations that Fh-like iron oxide patches grow pseudomorphically on pyrite surfaces when in contact with $O_2$ (*48*–*50*). Selected area electron diffraction (SAED) and HRTEM show that Fh in turn is enveloped by poorly crystalline Gth with a thickness of ~0.1 μm (Fig. 3, C and D, and fig. S6). We infer that Gth was formed directly from Fh because it is the more thermodynamically stable phase (*51*). This inference is consistent with laboratory observations that the initial oxidation products of pyrite are $Fe(OH)_3$ (ferrihydrite) followed by transformation to FeO(OH) (Gth) + $H_2O$, or FeO(OH) (feroxyhyte) followed by transformation to FeO(OH) (Gth) (*51*). The Fh-Gth sequence repeats in the outer layer (~0.9 μm in thickness), which is separated from the inner Fh-Gth sequence by a zone with low porosity, which is observed in the back-scattered electron micrograph as a dark zone (Fig. 3B).

This layering offers some insights into the reaction mechanism. Ferrihydrite or feroxyhite precipitates at near neutral or slightly acidic pH (*52*, *53*). This observation is important because it implies that the $H_2SO_4$ released during OWP does not drive pH far below neutral. We believe that the released acidity was likely consumed locally by dissolution of other minerals. Consistent with this inference, energy-dispersive x-ray spectra (EDS) of the Fe oxide layers reveal the presence of Si and Al (fig. S5). Because we observed chlorite dissolution initiating near OWP in several boreholes (*44*), we attribute the Si and Al to $H_2SO_4$-driven dissolution of local chlorite (Fig. 3A). Incorporation of silica into Fh also retards the transformation to Gth (*54*).

### The mechanism of oxidation is abiotic

Our observations are distinct from observations for weathering minerals of any composition in that we reported reaction fronts and weathering advance distances across scales from $10^{-9}$ to $10^{2}$ m, constraining the rate-limiting steps and reaction mechanisms. Furthermore, these results can probably be generalized because OWP occurs in rock at depth in very similar ways in other watersheds eroding at much faster rates in other climates (*30*–*35*, *38*).

The rate of OWP at Shale Hills is limited by diffusion of oxygen through shale matrix rather than chemical reaction. At the landscape scale, the rate is limited by movement of pyrite into the weathering zone, as dictated by the rate of erosion (*42*, *55*). Below the water table, we observed OWP only in halos around fractures (e.g., under the ridge) or where porosity is high because of carbonate dissolution under the valley (*44*). If transport of oxygen was not slow below the water table, then OWP would be extensive throughout the saturated zone. These observations point toward rate limitation at the clast scale by transport of oxygen, which is in turn limited by the formation of fractures and pores.

Oxidation is also not homogeneous at the grain scale (Fig. 3), suggesting that OWP is limited by transport of reactants or products through matrix to the grain surface. Transport cannot occur by advection at this scale because permeability, effective porosity, and total porosity are low in the shale matrix: In the protolith, these values are ~0.25 nanodarcy (*56*), 1.6 ± 0.5% (*30*), and 4.9 ± 0.4% (*30*), respectively. For most relatively unfractured low-porosity shales, reactants move by diffusion (*57*).

The observation that the rate-limiting step at the grain scale is diffusion through shale matrix is consistent with the pseudomorphic nature of the transformation and the sharp interface between pyrite and Fe oxide (Fig. 3A). Pseudomorphism is known to occur for some interfacial dissolution and reprecipitation reactions when the processes are slow and accompanied by small changes in volume (*58*, *59*). We calculated the transformation from Py to Fh to yield a 14% volume decrease (assuming Fe is immobile). This volume decrease could also contribute to the porosity, which is apparent as darker zones in the banded layers (Fig. 3B).

To constrain the mechanism, we consider three possible stoichiometries of OWP:

$$4FeS_2(s) + 15O_2(aq) + 14H_2O \rightarrow 8SO_4^{2-}(aq) + 16H^+(aq) + 4Fe(OH)_3(s) \quad \text{(Eq. 1)}$$

$$FeS_2(s) + 14Fe^{3+}(aq) + 8H_2O \rightarrow 2SO_4^{2-}(aq) + 16H^+(aq) + 15Fe^{2+}(aq) \quad \text{(Eq. 2)}$$

$$4FeS_2(s) + 7O_2(aq) + 10H_2O \rightarrow 4S_2O_3^{2-}(aq) + 8H^+(aq) + 4Fe(OH)_3(s) \quad \text{(Eq. 3)}$$

Fe(III) is the oxidant when aqueous Fe(III) is stable at the interface. In that case, the process is controlled by oxidation-reduction cycling

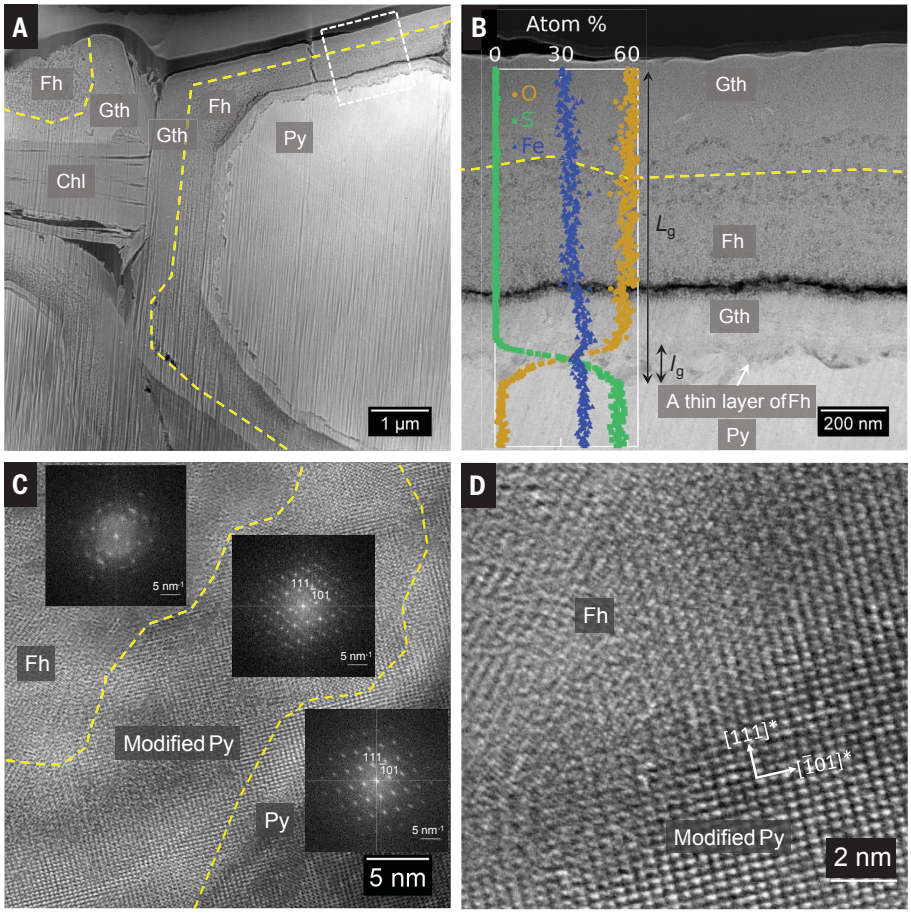


**Fig. 3. Pyrite oxidation at grain scale.** (**A**) Scanning TEM (STEM, HAADF mode) on a partially pseudomorphed pyrite grain identified using SEM-EDS (Fig. 2C) and then prepared by FIB. The dark gray rims are Fe oxides, and lighter gray core is pyrite. (**B**) STEM image showing the pyrite–Fe oxide interface [zoom-in view of the dashed box in (A)]. The colored lines show the elemental variations (normalized atomic percentage) versus distance, extracted from the line scan on the section. Mineral phases were identified from elemental composition (EDS) and electron diffraction. (**C**) HRTEM image showing the pyrite–Fe oxide interface with an inset showing a FFT of the modified pyrite region. (**D**) Zoomed-in view of modified Py-Fh interface. Chl: chlorite; Fh: ferrihydrite or feroxyhyte; Gth: goethite; Py: pyrite.

of Fe(II)-Fe(III) and can be accelerated by Fe-oxidizing microorganisms (*26*, *28*). However, the smallest bacteria reported in the subsurface are ~200 nm in nominal diameter (*60*), larger than the measured pore throats under the ridges (10 to 20 nm, table S1). Therefore, microorganisms are not likely to access the pyrite surface to accelerate the reactions. Alternatively, if thiosulfate formed as in (*3*), it could diffuse through the matrix out to the fractures and if sulfur-oxidizing microorganisms fit in the large fractures, then OWP could be mediated by thiosulfate-oxidizing organisms. This mechanism is also unlikely, however, because as a highly unstable molecule, thiosulfate is always observed at extremely low concentrations (*26*, *28*). Thus, OWP in this deep, low-porosity rock was not microbially catalyzed.

The mechanism is thus abiotic and is limited by diffusion with respect to either reactants or products. Neither diffusion of $H^+$ nor Fe(III) is likely limiting the rate given the circumneutral or slightly acidic pH near the Py-Fh interface. The lack of a sulfur-containing phase near the oxidized pyrite (Fig. 1C and fig. S5) also suggests that outward diffusion of sulfur species is not rate-limiting. Thus, inward diffusion of the oxidant must limit the rate.

At the near-neutral pH of the interface, aqueous Fe(III) is extremely low in concentration, and the oxidant is likely to be $O_2$ or nitrate. The latter oxidant may oxidize pyrite in nature but only if microorganisms participate. For example, sulfur-oxidizing, nitrate-reducing microorganisms are thought to accelerate OWP if they live directly on pyrite (*61*):

$$2FeS_2(s) + 6NO_3^-(aq) + 4H_2O \rightarrow 4SO_4^{2-}(aq) + 2H^+(aq) + 3N_2(g) + 2Fe(OH)_3(s) \quad \text{(Eq. 4)}$$

But nitrate as an oxidant is extremely unlikely because very little nitrate is observed in pore fluids at Shale Hills (*62*). We therefore conclude that OWP is abiotic and rate-limited by diffusion of oxygen through the shale matrix.

### Toward a multiscale model

Our observations show that oxygen, brought beneath the water table in fractures, diffuses into the matrix and oxidizes the pyrite. Microorganisms could be involved, but only to a very minor extent and only if they live in fractures rather than matrix or in a limited depth range under the valley where pore throats grow larger than micrometers (table S1). Above the water table, 100% of the pyrite oxidizes because the porosity is larger, the spacing between fractures is smaller (fig. S2), the fraction of air in the pores is higher, and the diffusion of oxygen is faster (*63*). Beneath the water table, OWP is restricted to a few larger, connected fracture zones under the ridge or to depth ranges where dissolution of carbonates has interconnected porosity under the valley (*44*). These arguments are consistent with simulations of weathering that show that a weathering front can locate either above or below the water table (*64*, *65*).

For the ridge boreholes where the OWP reaction front thickness $l_b$ is ~1 m (Fig. 1), a simple one-dimensional model based on water moving downward and rock moving upward is applicable. The average residence time $t_b$ for shale fragments crossing upward through the reaction front equals $l_b$ divided by the measured erosion rate of 0.02 ± 0.01 m $kyr^{-1}$ (*66*): 50 ± 30 thousand years (kyr). That is, fragments of shale (i.e., clasts) move up through the front over a period of 50 kyr while oxygen diffuses in from the fragment surface to oxidize the pyrite in the interior (fig. S4). At the point of exit from the top of the front after 50 kyr, each clast has become totally oxidized. At that point, the average distance that oxidation advances inward from each fracture, $L_c$, equals half the average fracture spacing $d_f$ (i.e., inverse of the fracture density, fig. S4).

The residence time during which each fragment crosses the front, 50 kyr, constrains the diffusion-limited oxidation rate of pyrite within each upward-transiting fragment, allowing parameterization of a diffusion model based on fracture spacing. We developed and corroborated such a model against published properties of shale and oxidation rates of pyrite (*67*). The most important model parameter is the effective diffusivity, $D_e$, which is smaller than aqueous diffusivity because of the low effective porosity ($\phi$) and tortuous pore pathways in the shale matrix (*68*). The most common empirical equation for $D_e$ is Archie's law, where it varies as $\phi^m$, $m$ being the cementation exponent. Using the constraint on $D_e$ from the diffusion model (where shale fragments completely oxidize within 50 kyr) and this empirical equation, we discover that the exponent $m$ constrained by our observations equals

literature values for shale (*67*). To further corroborate the diffusion model (*67*), we also calculated the average grain-scale oxidation rate of pyrite in the field of ~$10^{-14}$ mol $m^{-2}$ $s^{-1}$. This value is four orders of magnitude smaller than pyrite oxidation measured in the laboratory in well-stirred, slightly acidic water (*23*). This observation is consistent with rate limitation by diffusion in the field but interfacial reaction in the laboratory.

### Global implications

Our observations yield global implications for pyrite oxidation. For example, in some of the fastest-eroding locations on Earth, shales erode 10 to 100 times faster than at Shale Hills but still become 100% pyrite-oxidized beneath the land surface (*30*). Even in those fast-weathering shales, pyrite pseudomorphically transforms to oxide minerals (*30*). As shown by theoretical models of weathering (*10*, *42*, *55*), this observation implies that erosion limits the rate of OWP at the borehole scale rather than the kinetics of chemical reaction. In fact, by using reasonable parameters for average global pyrite contents and erosion rates, the calculated sulfate release rate for Shale Hills, 2.5 ± 1.4 mmol sulfur $m^{-2}$ $year^{-1}$, straightforwardly extrapolates to the total global riverine sulfate flux from OWP, 1.5 ± 0.5 Tmol sulfur $year^{-1}$ (*67*).

But to understand global implications over geological time, we also need to understand the mechanisms by which the rate of OWP at clast and grain scales varies proportionally with erosion rate. The answer appears to be that the climate, tectonic, or other drivers that accelerate the rates of erosion also promote increased fracturing (*69*). This in turn decreases the relevant clast size created between fractures (perhaps also increasing porosity within clasts) and thus accelerates OWP (*30*). This fits our proposed model (fig. S4) in which the advance of oxidation across each shale fragment between fractures is proportional to the square root of the residence time it takes for the fragment itself to cross the oxidation front. To fully oxidize pyrite in fragments, the fracture half-spacing must be less than the advance distance of oxidation as the clast crosses the reaction front at the borehole scale. A simple equation (eq. S10) predicts the critical fracture spacing that results in total oxidation of pyrite before it is exposed at the land surface and presents the spacing as a function of residence time of shale fragments in the weathering zone, effective porosity of shale matrix, pyrite abundance in protolith, and concentration of dissolved oxygen in fractures.

We used $m$ calculated from Shale Hills for three shales (*30*) for which we know that pyrite is oxidized before exposure at the land surface to determine the critical fracture spacing calculated from eq. S10 (Fig. 4). The measured fracture spacing and effective porosity for each of the shales plotted on the figure (symbols) show that fracture spacing is smaller than the critical spacing needed for 100% of the pyrite to be oxidized at the land surface under the present-day atmospheric level (PAL) of oxygen. The curves also show that the effect of fracture spacing is much stronger than that of porosity. These observations emphasize that the most convincing explanation for how OWP can be maintained proportional to erosion is that fracture spacing decreases to shorten the diffusion distance of oxygen as the erosion rate increases.

We can also explore conditions other than those on Earth today. For example, when the atmospheric oxygen concentration was less than $10^{-5}$ times PAL, OWP was apparently slow enough that pyrite was retained in alluvial sediments, implying that pyrite was exposed at the land surface [e.g., (*15*, *16*)]. Curves plotted for dissolved oxygen equilibrated with $PO_2$ = $10^{-5}$ PAL (Fig. 4) clearly show that even highly fractured rocks like those in fast-eroding Taiwan today would still retain pyrite up to the land surface at that time. This observation is consistent with a rate-limiting step for OWP before the GOE that was not erosion but rather the oxidation reaction at the mineral grain surface. Before the GOE, pyrite absence or presence in sediments would have been a function of atmospheric oxygen content, but once the atmospheric oxygen rose high enough to overcome chemical reaction limitation, OWP was limited by erosion and fracturing as it is today. Therefore, the key time scale for detrital pyrite preservation in alluvial sediments before the GOE is that of pyrite oxidation during transport from source to deposition as explored by Johnson *et al.* (2014) (*16*), but after the GOE the key time scale is the residence time as clasts transit up through the oxidation zone in the subsurface. This emphasizes that the rate of erosion coupled to fracturing in the subsurface is as important as atmospheric oxygen concentration in controlling the presence or absence of pyrite in alluvial material. Rock uplift and fracturing history, which has varied over geologic time (*70*), therefore must be considered in determining ancient atmospheric oxygen content through analyses of pyrite and models of weathering.

Our observations also emphasize that iron- and sulfur-oxidizing microorganisms do not play a dominant role today in OWP globally. This may explain why landscapes of acidification are generally limited to mined regions where pyrite-containing rock is artificially exposed. The only way microorganisms could play an important role, given that they need to grow directly on or near pyrite (*26*–*28*), is for pyrite to be exposed in rock where microorganisms can enter pores. However, pyrite would have been present at the land surface during the late Archaean even for very low erosion rates (see Fig. 4). This lends credence to the possibility that an early period of acidification at 2.48 Gyr ago was caused by chemolithoautotrophic bacteria colonizing the land surface where, unlike today, pyrite was exposed (*18*, *71*). More attention to estimating erosion rates and mechanics of subsurface fracturing is needed to understand limits on C, O, S, and Fe cycles globally.

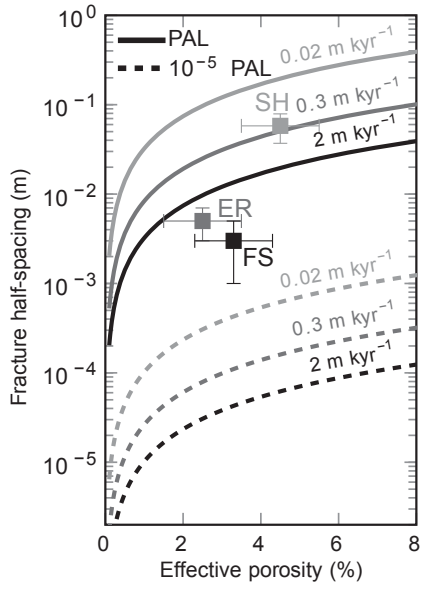


**Fig. 4. Model curves showing the critical values of fracture half-spacing and effective porosity for pyrite to completely oxidize (symbols plot below curve) or to remain unoxidized at Earth's surface (symbols plot above curve) for two values of atmospheric oxygen.** Squares show fracture half-spacing and effective porosity measured from depth at three watersheds (SH: Shale Hills at Pennsylvania; ER: Eel River at California; FS: Fushan at Taiwan) with different erosion rates. Darker symbols and curves indicate faster erosion rates as labeled: FS (2 m $kyr^{-1}$) > ER (0.3 m $kyr^{-1}$) > SH (0.02 m $kyr^{-1}$). Solid and dashed curves were calculated for oxygen at present atmospheric levels (PAL) or levels from before the GOE ($10^{-5}$ PAL), respectively. Consistent with today's lack of exposed pyrite at land surface in all three watersheds and sulfate release rates for the watersheds that are proportional to erosion rate (*30*), symbols all plot below the corresponding contour for PAL (erosion-limited oxidation). But all points plot above estimates based on $10^{-5}$ PAL (dashed lines), suggesting the likelihood of land surface exposure of pyrite before the GOE (reaction-limited oxidation). Parameters estimated from Shale Hills were applied to the other watersheds as described in the text. Error bars show the range of erosion rates (horizontal) and fracture half-spacing (vertical). The contours of different values of erosion rates (darker for higher erosion rate) are calculated using eq. S10 for a 10-m-thick oxidized regolith.

## Materials and methods

### Geological setting

The Shale Hills catchment (40.6668° N, 77.9028° W) at Susquehanna Shale Hills Critical Zone Observatory (SSHCZO) is a V-shaped 0.08 $km^2$ catchment located in the headwaters of the Shaver's Creek watershed in the central Susquehanna River Basin, Pennsylvania, USA (fig. S1). The climate at SSHCZO is characterized as humid continental, with warm to hot summers and cold winters (mean annual air temperature of 10°C), with well-distributed precipitation throughout the year (mean annual precipitation of 107 cm). Vegetative cover is dominated by northern hardwoods with interspersed conifers consisting of oak (*Quercus spp.*), hickory (*Carya spp.*), pine (*Pinus spp.*), hemlock (*Tsuga canadensis*), and red maple (*Acer rubrum*). The short-term erosion rate (0.01 to 0.025 mm $year^{-1}$) determined from meteoric $^{10}Be$ in this catchment (*66*) is comparable to the long-term erosion rates determined by low-temperature thermochronometry (*72*) across the Valley and Ridge province, in the Appalachian Mountain region. Both rates are close to the soil production rate (0.015 to 0.065 mm $year^{-1}$) determined over the $10^3$- to $10^4$-year time scale from uranium disequilibrium isotopes (*73*). This similarity implies that the landscape is close to an approximate steady-state geomorphological shape, i.e., that erosion roughly balances soil production. This site is underlain by the Silurian-aged Rose Hill Formation, which consists primarily of shale with minor interbedded carbonate-rich and sandstone layers (*37*, *74*). The shale under the catchment varies from carbonate-rich near the outlet to poor through the rest of the catchment. Carbonate layers in the dipping (and probably folded) shale intersect boreholes under the ridges at tens of meters below land surface but at ~2 mbls under the valley. Although most carbonate at depth under the valley was present in the original shale, some calcite precipitated near the surface (<3 mbls) shows incorporation of C from organic carbon in soil, which is isotopically more depleted (*44*).

### Boreholes

A 7.6-cm-diameter borehole (CZMW8) was drilled to 30.8-m depth under the south ridge of the catchment by HQ wireline coring, and core materials were recovered. Above depths of ~15.5 m, fractured rock fragments with lengths smaller than 10 cm were recovered (recovery: 17 to 40%). Below ~15.5 m, more continuous core materials were recovered (recovery: 45 to 90%) with the exception of the highly fractured zone from 24.7 to 26.2 m (recovery: 21%).

A 7.6-cm-diameter borehole (CZMW10) was drilled to 35-m depth under the valley near the outlet of the catchment by air rotary drilling. Rock fragments and rock powder were sampled during drilling at ~0.8-m intervals. The unconsolidated material in the top 3 m of the borehole was sampled using a Geoprobe. The groundwater levels of these two boreholes are continuously measured every 30 min using a pressure transducer after well completion (*75*).

The borehole geophysical logs collected in both borehole CZMW8 and CZMW10 include a three-arm caliper, natural gamma, optical televiewer, acoustic televiewer, full wave-form sonic, bulk density, neutron porosity, fluid temperature, fluid conductivity, and normal resistivity. The logs of the 3-arm caliper and optical televiewer were collected in several other boreholes under the ridge (CZMW5, CZMW6, CZMW7) and under the valley as well (boreholes: CZMW1, CZMW2, CZMW3, CZMW4, Lynch). The fracture density was estimated by counting numbers of fractures per 0.5 m on optical and acoustic borehole images.

### Bulk chemistry and minerology

Two types of samples were collected for analysis: (i) bulk samples (>100 g each), collected and homogenized over 0.3- to 0.8-m depth intervals; and (ii) centimeter-sized rock fragments that could be separated, on occasion, from the bulk samples. Rock fragments analyzed and discussed in this paper were collected near the depth where almost all of the pyrite becomes depleted (the pyrite oxidation front), or from the fractured zones (3 to 20 g for each sample). Bulk solid-state elemental compositions were determined by lithium metaborate fusion followed by inductively coupled plasma–atomic emission spectroscopy (ICP-AES; Perkin-Elmer Optima 5300DV ICP-AES) at the Penn State Laboratory for Isotopes and Metals in the Environment (LIME). Loss on ignition was determined by ashing the pulverized samples (initial mass ~1 g) at 900°C for 1 hour. Concentrations of total carbon and sulfur were determined on pulverized samples with a combustion–infrared carbon/sulfur determinator (LECO SC632). Bulk compositions are reported on an "as received" basis.

The loss or gain of component $j$ during weathering was quantified as the mass transfer coefficient $\tau_j$ (*76*, *77*):

$$\tau_j = \frac{C_{j,w}C_{i,p}}{C_{j,p}C_{i,w}} - 1$$

Here, $C_{j,w}$ and $C_{j,p}$ are the concentrations of a mobile element or mineral of interest ($j$) in protolith ($p$) or weathered material ($w$). When $\tau = 0$, element $j$ is neither enriched nor depleted with respect to immobile element $i$ in protolith; when $\tau < 0$, the element has been lost relative to $i$ in protolith; and when $\tau > 0$, the element has been added to the profile relative to the protolith. In this study, the protolith is defined as the zone that shows no pyrite or carbonate depletion and titanium (Ti) is chosen as the immobile element because it is mostly present in an insoluble mineral (*30*). The fraction of a mobile element lost from the protolith is a minimum estimate because no element is totally immobile (*78*). The extent of oxidation was calculated as $-\tau_{py}$.

X-ray diffraction was conducted on a PANalytical Empyrean X-Ray Diffractometer (PANalytical Ltd., Netherlands) at 45 kV and 40 mA using Cu $K\alpha$ radiation with a 1/2° divergence and receiving slits. Diffraction profiles were collected from 5° to 70° 2θ at a rate of 4° $min^{-1}$. The degree of vermiculitization of chlorite was semiquantitatively estimated through the relative intensities of the (002) reflection at ~7.1 Å and (001) reflection at 14.1 to 14.3 Å of chlorite (*79*).

### SEM

Eleven centimeter-sized rock fragments from different depths were selected for microstructure analysis at the Material Characterization Laboratory of the Pennsylvania State University. All fragments were cut into thin sections (~2 mm thick) using a low-speed diamond saw, polished with sandpaper (600 grid) and later diamond pastes (6 μm and 0.25 μm). Thin sections from each depth were imaged by scanning electron microscope (SEM). Selected sections were further polished by an ion beam milling instrument (Leica EM TIC 3X) to reveal the internal structure. Before imaging, the sections were coated with carbon (~8 nm thick) to reduce surface charging. The sections were imaged at low magnification (<10,000×) using an Environmental SEM (FEI Quanta 250) in backscattered electron mode with an accelerating voltage of 10 to 15 kV. Selected areas were investigated by EDS on the SEM using an Oxford EDS detector with an accelerating voltage of 15 to 20 kV to ensure a minimum dead time of 15%. The sections were imaged at high magnification (>10,000×) using a field-emission SEM (FEI Nova NanoSEM 630) with an accelerating voltage of 8 to 10 kV, landing energy of 4 to 5 kV using a vCD detector.

### TEM

Specimens for transmission electron microscopy (TEM) were prepared by focused ion beam (FIB) milling on specific sites (e.g., pyrite-Fe oxide interface pre-identified by SEM-EDS) with the FEI Helios NanoLab 660 DualBeam system. A protective carbon layer was deposited on the region in the shape of a bar and then milling was performed using gallium ions at 30 keV. The specimen was lifted out, attached to a TEM grid and thinned to electron transparency. The FIB specimen was then analyzed on a Talos F200X scanning/transmission electron microscope (S/TEM) or a FEI Titan3 dual aberration corrected S/TEM, both operated at 200 kV and equipped with a SuperX EDS system. Both high angle annular dark field

(HAADF) STEM imaging and HRTEM were completed. Selected areas were examined by SAED and EDS mapping. Electron diffraction patterns were also extracted through fast Fourier transform (FFT) analysis on selected area of HRTEM images using image processing software Fiji (*80*). The ion mill curtaining in Fig. 3A is removed by a stripe filtering plugin in Fiji (*81*).

## REFERENCES AND NOTES


1. D. Rickard, G. W. Luther 3rd, Chemistry of iron sulfides. *Chem. Rev.* **107**, 514–562 (2007). doi: 10.1021/cr0503658; pmid: 17261073
2. H. D. Holland, The chemistry of the atmosphere and oceans (John Wiley & Sons, NY, 1978).
3. L. R. Kump, R. M. Garrels, Modeling atmospheric $O_2$ in the global sedimentary redox cycle. *Am. J. Sci.* **286**, 337–360 (1986). doi: 10.2475/ajs.286.5.337
4. R. A. Berner, D. E. Canfield, A new model for atmospheric oxygen over Phanerozoic time. *Am. J. Sci.* **289**, 333–361 (1989). doi: 10.2475/ajs.289.4.333; pmid: 11539776
5. R. A. Berner, GEOCARBSULF: A combined model for Phanerozoic atmospheric $O_2$ and $CO_2$. *Geochim. Cosmochim. Acta* **70**, 5653–5664 (2006). doi: 10.1016/j.gca.2005.11.032
6. R. Raiswell, D. E. Canfield, The iron biogeochemical cycle past and present. *Geochem. Perspect.* **1**, 1–220 (2012). doi: 10.7185/geochempersp.1.1
7. A. Burke *et al*., Sulfur isotopes in rivers: Insights into global weathering budgets, pyrite oxidation, and the modern sulfur cycle. *Earth Planet. Sci. Lett.* **496**, 168–177 (2018). doi: 10.1016/j.epsl.2018.05.022
8. D. R. Lovley, Microbial Fe(III) reduction in subsurface environments. *FEMS Microbiol. Rev.* **20**, 305–313 (1997). doi: 10.1111/j.1574-6976.1997.tb00316.x
9. H. Prommer, P. J. Stuyfzand, Identification of temperature-dependent water quality changes during a deep well injection experiment in a pyritic aquifer. *Environ. Sci. Technol.* **39**, 2200–2209 (2005). doi: 10.1021/es0486768; pmid: 15871255
10. E. W. Bolton, R. A. Berner, S. T. Petsch, The weathering of sedimentary organic matter as a control on atmospheric $O_2$: II. Theoretical modeling. *Am. J. Sci.* **306**, 575–615 (2006). doi: 10.2475/08.2006.01
11. A. Lerman, L. L. Wu, F. T. Mackenzie, $CO_2$ and $H_2SO_4$ consumption in weathering and material transport to the ocean, and their role in the global carbon balance. *Mar. Chem.* **106**, 326–350 (2007). doi: 10.1016/j.marchem.2006.04.004
12. M. A. Torres, A. J. West, G. Li, Sulphide oxidation and carbonate dissolution as a source of $CO_2$ over geological timescales. *Nature* **507**, 346–349 (2014). doi: 10.1038/nature13030; pmid: 24646998
13. D. E. Canfield, The early history of atmospheric oxygen: Homage to Robert A. Garrels. *Annu. Rev. Earth Planet. Sci.* **33**, 1–36 (2005). doi: 10.1146/annurev.earth.33.092203.122711
14. T. W. Lyons, C. T. Reinhard, N. J. Planavsky, The rise of oxygen in Earth's early ocean and atmosphere. *Nature* **506**, 307–315 (2014). doi: 10.1038/nature13068; pmid: 24553238
15. B. Rasmussen, R. Buick, Redox state of the Archean atmosphere: Evidence from detrital heavy minerals in ca. 3250–2750 Ma sandstones from the Pilbara Craton, Australia. *Geology* **27**, 115–118 (1999). doi: 10.1130/0091-7613(1999)027<0115:RSOTAA>2.3.CO;2
16. J. E. Johnson, A. Gerpheide, M. P. Lamb, W. W. Fischer, $O_2$ constraints from Paleoproterozoic detrital pyrite and uraninite. *Geol. Soc. Am. Bull.* **126**, 813–830 (2014). doi: 10.1130/B30949.1
17. A. Bekker, H. D. Holland, Oxygen overshoot and recovery during the early Paleoproterozoic. *Earth Planet. Sci. Lett.* **317-318**, 295–304 (2012). doi: 10.1016/j.epsl.2011.12.012
18. K. O. Konhauser *et al*., Aerobic bacterial pyrite oxidation and acid rock drainage during the Great Oxidation Event. *Nature* **478**, 369–373 (2011). doi: 10.1038/nature10511; pmid: 22012395
19. D. E. Canfield, Oxygen: A four billion year history (Princeton University Press, 2014).
20. S. J. Daines, B. J. W. Mills, T. M. Lenton, Atmospheric oxygen regulation at low Proterozoic levels by incomplete oxidative weathering of sedimentary organic carbon. *Nat. Commun.* **8**, 14379 (2017). doi: 10.1038/ncomms14379; pmid: 28148950
21. C. O. Moses, D. Kirk Nordstrom, J. S. Herman, A. L. Mills, Aqueous pyrite oxidation by dissolved-oxygen and by ferric iron. *Geochim. Cosmochim. Acta* **51**, 1561–1571 (1987). doi: 10.1016/0016-7037(87)90337-1
22. M. A. Williamson, J. D. Rimstidt, The kinetics and electrochemical rate-determining step of aqueous pyrite oxidation. *Geochim. Cosmochim. Acta* **58**, 5443–5454 (1994). doi: 10.1016/0016-7037(94)90241-0
23. A. C. Johnson *et al*., Experimental determination of pyrite and molybdenite oxidation kinetics at nanomolar oxygen concentrations. *Geochim. Cosmochim. Acta* **249**, 160–172 (2019). doi: 10.1016/j.gca.2019.01.022
24. P. C. Singer, W. Stumm, Acidic mine drainage: The rate-determining step. *Science* **167**, 1121–1123 (1970). doi: 10.1126/science.167.3921.1121; pmid: 17829406
25. D. W. Blowes, C. J. Ptacek, J. L. Jambor, C. G. Weisener, The geochemistry of acid mine drainage, in *Treatise on Geochemistry. Vol. 9. Environmental Geochemistry* B. Sherwood Lollar (Ed.) (Elsevier, Toronto, 2003), pp. 149–204.
26. W. Sand, T. Gerke, R. Hallmann, A. Schippers, Sulfur chemistry, biofilm, and the (in)direct attack mechanism – a critical evaluation of bacterial leaching. *Appl. Microbiol. Biotechnol.* **43**, 961–966 (1995). doi: 10.1007/BF00166909
27. M. Gleisner, R. B. Herbert Jr., P. C. Frogner Kockum, Pyrite oxidation by Acidithiobacillus ferrooxidans at various concentrations of dissolved oxygen. *Chem. Geol.* **225**, 16–29 (2006). doi: 10.1016/j.chemgeo.2005.07.020
28. E. Percak-Dennett *et al*., Microbial acceleration of aerobic pyrite oxidation at circumneutral pH. *Geobiology* **15**, 690–703 (2017). doi: 10.1111/gbi.12241; pmid: 28452176
29. D. Calmels, J. Gaillardet, A. Brenot, C. France-Lanord, Sustained sulfide oxidation by physical erosion processes in the Mackenzie River basin: Climatic perspectives. *Geology* **35**, 1003–1006 (2007). doi: 10.1130/G24132A.1
30. X. Gu *et al*., Chemical reactions, porosity, and microfracturing in shale during weathering: The effect of erosion rate. *Geochim. Cosmochim. Acta* **269**, 63–100 (2020). doi: 10.1016/j.gca.2019.09.044
31. R. Littke, U. Klussmann, B. Krooss, D. Leythaeuser, Quantification of loss of calcite, pyrite, and organic matter due to weathering of Toarcian black shales and effects on kerogen and bitumen characteristics. *Geochim. Cosmochim. Acta* **55**, 3369–3378 (1991). doi: 10.1016/0016-7037(91)90494-P
32. R. A. Wildman *et al*., The weathering of sedimentary organic matter as a control on atmospheric $O_2$: I. Analysis of a black shale. *Am. J. Sci.* **304**, 234–249 (2004). doi: 10.2475/ajs.304.3.234
33. L. X. Jin *et al*., Evolution of porosity and geochemistry in Marcellus Formation black shale during weathering. *Chem. Geol.* **356**, 50–63 (2013). doi: 10.1016/j.chemgeo.2013.07.012
34. J. Wan *et al*., Predicting sedimentary bedrock subsurface weathering fronts and weathering rates. *Sci. Rep.* **9**, 17198 (2019). doi: 10.1038/s41598-019-53205-2; pmid: 31748585
35. M. Chigira, T. Oyama, Mechanism and effect of chemical weathering of sedimentary rocks. *Eng. Geol.* **55**, 3–14 (2000). doi: 10.1016/S0013-7952(99)00102-7
36. S. L. Brantley, M. E. Holleran, L. X. Jin, E. Bazilevskaya, Probing deep weathering in the Shale Hills Critical Zone Observatory, Pennsylvania (USA): The hypothesis of nested chemical reaction fronts in the subsurface. *Earth Surf. Process. Landf.* **38**, 1280–1298 (2013). doi: 10.1002/esp.3415
37. P. L. Sullivan *et al*., Oxidative dissolution under the channel leads geomorphological evolution at the Shale Hills catchment. *Am. J. Sci.* **316**, 981–1026 (2016). doi: 10.2475/10.2016.02
38. C. Lerouge *et al*., A deep alteration and oxidation profile in a shallow clay aquitard: Example of the Tégulines Clay, East Paris Basin, France. *Geofluids* **2018**, 1606753 (2018). doi: 10.1155/2018/1606753
39. H. Drake, E.-L. Tullborg, A. B. MacKenzie, Detecting the near-surface redox front in crystalline bedrock using fracture mineral distribution, geochemistry and U-series disequilibrium. *Appl. Geochem.* **24**, 1023–1039 (2009). doi: 10.1016/j.apgeochem.2009.03.004
40. S. L. Brantley, M. Lebedeva, E. Bazilevskaya, Relating weathering fronts for acid neutralization and oxidation to $pCO_2$ and $pO_2$, in *Treatise on Geochemistry*, J. Farquhar, J. Kasting, D. Canfield, Eds. (Elsevier, ed. 2, 2013), vol. 6, pp. 327–352.
41. S. L. Brantley *et al*., Susquehanna Shale Hills Critical Zone Observatory: Shale Hills in the context of Shaver's Creek watershed. *Vadose Zone J.* **17**, 180092 (2018). doi: 10.2136/vzj2018.04.0092
42. M. I. Lebedeva, R. C. Fletcher, S. L. Brantley, A mathematical model for steady-state regolith production at constant erosion rate. *Earth Surf. Process. Landf.* **35**, 508–524 (2010). doi: 10.1002/esp.1954
43. C. S. Riebe, W. J. Hahm, S. L. Brantley, Controls on deep critical zone architecture: A historical review and four testable hypotheses. *Earth Surf. Process. Landf.* **42**, 128–156 (2017). doi: 10.1002/esp.4052
44. X. Gu *et al*., Seismic refraction tracks porosity generation and possible $CO_2$ production at depth under a headwater catchment. *Proc. Natl. Acad. Sci. U.S.A.* **117**, 18991–18997 (2020). pmid: 32719121
45. A. H. Thompson, A. J. Katz, C. E. Krohn, The microgeometry and transport properties of sedimentary rock. *Adv. Phys.* **36**, 625–694 (1987). doi: 10.1080/00018738700101062
46. J. K. Fredrickson *et al*., Pore-size constraints on the activity and survival of subsurface bacteria in a late Cretaceous shale-sandstone sequence, northwestern New Mexico. *Geomicrobiol. J.* **14**, 183–202 (1997). doi: 10.1080/01490459709378043
47. A. Navarre-Sitchler, S. L. Brantley, Basalt weathering across scales. *Earth Planet. Sci. Lett.* **261**, 321–334 (2007). doi: 10.1016/j.epsl.2007.07.010
48. C. M. Eggleston, J.-J. Ehrhardt, W. Stumm, Surface structural controls on pyrite oxidation kinetics: An XPS-UPS, STM, and modeling study. *Am. Mineral.* **81**, 1036–1056 (1996). doi: 10.2138/am-1996-9-1002
49. K. M. Rosso, U. Becker, M. F. Hochella, The interaction of pyrite 100 surfaces with $O_2$ and $H_2O$: Fundamental oxidation mechanisms. *Am. Mineral.* **84**, 1549–1561 (1999). doi: 10.2138/am-1999-1008
50. C. Mahoney, C. März, J. Buckman, T. Wagner, V.-O. Blanco-Velandia, Pyrite oxidation in shales: Implications for palaeo-redox proxies based on geochemical and SEM-EDX evidence. *Sediment. Geol.* **389**, 186–199 (2019). doi: 10.1016/j.sedgeo.2019.06.006
51. R. M. Cornell, U. Schwertmann, *The Iron Oxides: Structure, Properties, Reactions, Occurrence, and Uses* (VCH, 1996).
52. F. V. Chukhrov *et al*., Feroxyhyte, a new modification of FeOOH. *Int. Geol. Rev.* **19**, 873–890 (1977). doi: 10.1080/00206817709471086
53. J. L. Jambor, J. E. Dutrizac, Occurrence and constitution of natural and synthetic ferrihydrite, a widespread iron oxyhydroxide. *Chem. Rev.* **98**, 2549–2586 (1998). doi: 10.1021/cr970105t; pmid: 11848971
54. R. M. Cornell, R. Giovanoli, P. W. Schindler, Effect of silicate species on the transformation of ferrihydrite into goethite and hematite in alkaline media. *Clays Clay Miner.* **35**, 21–28 (1987). doi: 10.1346/CCMN.1987.0350103
55. A. J. West, A. Galy, M. Bickle, Tectonic and climatic controls on silicate weathering. *Earth Planet. Sci. Lett.* **235**, 211–228 (2005). doi: 10.1016/j.epsl.2005.03.020
56. B. W. Kuntz, S. Rubin, B. Berkowitz, K. Singha, Quantifying solute transport at the Shale Hills Critical Zone Observatory. *Vadose Zone J.* **10**, 843–857 (2011). doi: 10.2136/vzj2010.0130
57. P. M. Jardine *et al*., Quantifying diffusive mass transfer in fractured shale bedrock. *Water Resour. Res.* **35**, 2015–2030 (1999). doi: 10.1029/1999WR900043
58. A. Putnis, Mineral Replacement Reactions. *Rev. Mineral. Geochem.* **70**, 87–124 (2009). doi: 10.2138/rmg.2009.70.3
59. R. Hellmann *et al*., Unifying natural and laboratory chemical weathering with interfacial dissolution–reprecipitation: A study based on the nanometer-scale chemistry of fluid-silicate interfaces. *Chem. Geol.* **294-295**, 203–216 (2012). doi: 10.1016/j.chemgeo.2011.12.002
60. B. Luef *et al*., Diverse uncultivated ultra-small bacterial cells in groundwater. *Nat. Commun.* **6**, 6372 (2015). doi: 10.1038/ncomms7372; pmid: 25721682
61. J. Bosch, K. Y. Lee, G. Jordan, K. W. Kim, R. U. Meckenstock, Anaerobic, nitrate-dependent oxidation of pyrite nanoparticles by Thiobacillus denitrificans. *Environ. Sci. Technol.* **46**, 2095–2101 (2012). doi: 10.1021/es2022329; pmid: 22142180
62. J. N. Weitzman, J. P. Kaye, Nitrogen budget and topographic controls on nitrous oxide in a shale-based watershed. *J. Geophys. Res. Biogeosci.* **123**, 1888–1908 (2019). doi: 10.1029/2017JG004344
63. F. Callebaut, D. Gabriels, W. Minjauw, M. D. E. Boodt, Redox potential, oxygen diffusion rate, and soil gas composition in relation to water table level in two soils. *Soil Sci.* **134**, 149–156 (1982). doi: 10.1097/00010694-198209000-00001
64. M. I. Lebedeva, S. L. Brantley, Relating the depth of the water table to the depth of weathering. *Earth Surf. Process. Landf.* **45**, 2167–2178 (2020). doi: 10.1002/esp.4873
65. Y. Kanzaki, S. L. Brantley, L. R. Kump, A numerical examination of the effect of sulfide dissolution on silicate weathering. *Earth Planet. Sci. Lett.* **539**, 116239 (2020). doi: 10.1016/j.epsl.2020.116239

66. N. West *et al*., Regolith production and transport at the Susquehanna Shale Hills Critical Zone Observatory, Part 2: Insights from meteoric $^{10}$Be. *J. Geophys. Res. Earth Surf.* **118**, 1877–1896 (2013). doi: 10.1002/jgrf.20121
67. Details about the model are available as supplementary materials.
68. P. Grathwohl, Diffusion in natural porous media: Contaminant transport, sorption/desorption and dissolution kinetics (Springer, 1998)
69. P. Molnar, R. S. Anderson, S. P. Anderson, Tectonics, fracturing of rock, and erosion. *J. Geophys. Res. Earth Surf.* **112**, F03014 (2007).
70. C. Hawkesworth, P. A. Cawood, B. Dhuime, Rates of generation and growth of the continental crust. *Geoscience Frontiers* **10**, 165–173 (2019). doi: 10.1016/j.gsf.2018.02.004
71. E. E. Stüeken, D. C. Catling, R. Buick, Contributions to late Archaean sulphur cycling by life on land. *Nat. Geosci.* **5**, 722–725 (2012). doi: 10.1038/ngeo1585
72. M. K. Roden, D. S. Miller, Apatite fission-track thermochronology of the Pennsylvania Appalachian Basin. *Geomorphology* **2**, 39–51 (1989). doi: 10.1016/0169-555X(89)90005-6
73. L. Ma *et al*., Regolith production and transport in the Susquehanna Shale Hills Critical Zone Observatory, Part 1: Insights from U-series isotopes. *J. Geophys. Res. Earth Surf.* **118**, 722–740 (2013). doi: 10.1002/jgrf.20037
74. L. X. Jin *et al*., Mineral weathering and elemental transport during hillslope evolution at the Susquehanna/Shale Hills Critical Zone Observatory. *Geochim. Cosmochim. Acta* **74**, 3669–3691 (2010). doi: 10.1016/j.gca.2010.03.036
75. Data are available at http://www.czo.psu.edu/data_time_series.html.
76. G. H. Brimhall, W. E. Dietrich, Constitutive mass balance relations between chemical-composition, volume, density, porosity, and strain in metasomatic hydrochemical systems: Results on weathering and pedogenesis. *Geochim. Cosmochim. Acta* **51**, 567–587 (1987). doi: 10.1016/0016-7037(87)90070-6
77. S. P. Anderson, W. E. Dietrich, G. H. Brimhall Jr., Weathering profiles, mass-balance analysis, and rates of solute loss: Linkages between weathering and erosion in a small, steep catchment. *Geol. Soc. Am. Bull.* **114**, 1143–1158 (2002). doi: 10.1130/0016-7606(2002)114<1143:WPMBAA>2.0.CO;2
78. H. Kim, X. Gu, S. L. Brantley, Particle fluxes in groundwater change subsurface shale rock chemistry over geologic time. *Earth Planet. Sci. Lett.* **500**, 180–191 (2018). doi: 10.1016/j.epsl.2018.07.031
79. C. E. Weaver, The distribution and identification of mixed-layer clays in sedimentary rocks. *Clays Clay Miner.* **4**, 385–386 (1955). doi: 10.1346/CCMN.1955.0040143
80. J. Schindelin *et al*., Fiji: An open-source platform for biological-image analysis. *Nat. Methods* **9**, 676–682 (2012). doi: 10.1038/nmeth.2019; pmid: 22743772
81. B. Münch, P. Trtik, F. Marone, M. Stampanoni, Stripe and ring artifact removal with combined wavelet—Fourier filtering. *Opt. Express* **17**, 8567–8591 (2009). doi: 10.1364/OE.17.008567; pmid: 19434191
82. Data are available at www.czo.psu.edu/data_geochemical_geophysical.html.

## ACKNOWLEDGMENTS

We thank B. Watson, E. Roden, and M. Lebedeva for insights. The paper benefitted greatly from the reviews provided by A. Johnson, K. Konhauser, and an anonymous reviewer. **Funding:** Financial support was provided by U.S. DOE grant OBES DE-FG02-05ER15675 (S.L.B.), National Science Foundation grants EAR–1239285 and EAR–1331726 (S.L.B.), and EAR-1925903 (P.J.H.). F.D.A.A.R. acknowledges support from Brazilian agencies FAPERJ (E-26/202.881/2018), CAPES (88887.310427/2018-00), and CNPq (304766/2014-3). This research was conducted in Penn State's Stone Valley Forest, which is funded by the Penn State College of Agriculture Sciences, Department of Ecosystem Science and Management, and managed by the staff of the Forestlands Management Office. **Author contributions:** S.L.B. and X.G. conceived and led the project. X.G. collected the samples and conducted measurements. X.G. and P.J.H. interpreted mineralogical data. X.G. and F.D.A.A.R. developed the multiscale model. X.G. and S.L.B. wrote the paper, with input from all authors; **Competing interests:** The authors declare that they have no competing interests. **Data and materials availability:** Data are available in supplementary materials. Borehole logging data are available at the CZO data repository (*82*).

## SUPPLEMENTARY MATERIALS

science.sciencemag.org/content/370/6515/eabb8092/suppl/DC1
Supplementary Text
Figs. S1 to S7
Tables S1 and S2
References (*83*–*97*)

20 March 2020; accepted 17 August 2020
10.1126/science.abb8092

Science

# Deep abiotic weathering of pyrite

Xin Gu, Peter J. Heaney, Fabio D. A. Aarão Reis and Susan L. Brantley

*Science* **370** (6515), eabb8092.
DOI: 10.1126/science.abb8092

**Getting rid of fool's gold**

Pyrite, also called fool's gold, is an iron sulfide mineral that is very commonly found in rock but is almost nonexistent in sediments today. Pyrite oxidizes quickly and is a major source of sulfur to the ocean, but it is also a proxy for the oxygen content historically in Earth's atmosphere. Gu *et al.* conducted a set of detailed observations of the pyrite oxidation process in a shale unit. The authors found that erosion tied to fracturing is just as important as the oxygen content for the dissolution process. They developed a model that helps determine the conditions in Earth's past for which pyrite might have been stable and the role of microorganisms in the oxidation process.

*Science*, this issue p. eabb8092



*Science* (print ISSN 0036-8075; online ISSN 1095-9203) is published by the American Association for the Advancement of Science, 1200 New York Avenue NW, Washington, DC 20005. The title *Science* is a registered trademark of AAAS.